Design and Control of a New 3-PUU Fast Tool Servo for Complex Microstructure Machining

Hui Tang[#*1], Hongcheng Li[#1], Suet To[2], Kai-Ming Yu[2], Yunbo He[*1], Jian Gao[1], Xin Chen[1], Jiedong Li[1]

[1]Key Laboratory of Precision Microelectronic Manufacturing Technology & Equipment of Ministry of Education
Guangdong University of Technology, Higher Education Mega Center, Guangzhou, China.

[2] The Department of Industrial and Systems Engineering
The Hong Kong Polytechnic University, Hung Hom, Kowloon, Hong Kong SAR, China.

*Corresponding author: Email: huitang@gdut.edu.cn (Hui Tang); 2763661825@qq.com (Yunbo He)

Abstract—Ultra-precision fast tool servo(FTS) machining technology is an effective method for complex surface microstructure machining. However, as for a single degree-of-freedom (DOF) FTS, it can only achieve a high-rate reciprocating movement in one direction, thus it can't realize ultra-precision machining for some complex microstructural surface. Therefore, a novel flexure-based fast tool servo device composed of two platforms and three branched chains is proposed in this work, which aims to realize a robotic ultra-precision machining with XYZ translational precision motion. Each of the branched chain is made up of a prismatic pair, two hook hinges and a connecting rod. The FTS mechanism design and modeling are carried out firstly; then, the FTS device characterization in terms of statics analysis and modal analysis are conducted; in order to suppress the hysteresis nonlinearity and improve the positioning precision, a new repetitive-compensated PID controller combined with an inverted modified Prandtl-Ishlinskii model is proposed to handle this issue. It indicates that the displacement amplification ratio is 3.87, thus the workspace can reach to $[-85, 85]\cup[-80,80]\cup[0,120]\mu m^3$, the closed-loop positioning precision is 600nm, which will be considered to fulfill practical FTS machining tasks.

Keywords Fast tool servo · Microstructure · Ultra-precision machining · Flexure · Hysteresis model

1 Introduction

Microstructure surface is a small topological shape on the surface of a specific function with sub-micron surface shape accuracy and nanoscale surface roughness. It is got high attention and widely used in many fields because of its small volume, light quality, and low cost, and it can realize common element is difficult to implement new functionality such as array, integration [1-5]. However, microstructure surface is axisymmetric, irregular surface with high machining precision requirement and its shape is very complicated. Microstructure surface machining has always been a big problem on a global scale. The traditional machining methods due to the low efficiency and low precision, it is difficult to meet the machining requirements. A number of new machining methods have been proposed and applied to microstructure surface machining [6-10]. FTS machining technology, because of its characteristics of high frequency and high precision, high efficiency, is generally accepted the most suitable microstructure surface machining methods [11,12].

The principle of FTS is: by adding the servo device which can achieve the reciprocating motion in high frequency, the cutting tools following the spindle achieve high frequency motion synchronously, besides moving with the motion of lathe [13,14]. The FTS mainly includes three parts: the driving device, guiding mechanism and position measurement. The FTS with all kinds of driving principles and guiding mechanisms is studied frequently by the researchers around the world. However, most of the researchers pay attention to single DOF FTS at present, and the single DOF FTS is defective in machining complex precision surface.

Some scholars put forward the multi-DOF FTS which can achieve active cutting in multiple direction, displacement compensation in multiple direction, solve the issue of cutting force and so on [15,16]. The multi-DOF FTS ensure the synchronism and harmony of the motion which is following the spindle and overcome the problems of single DOF FTS machining. Besides, it enlarges the machining range of the complex surface and microstructure and strengthen the ability of machining. The FTS with more DOF can achieve the machining which can't be finished or hard to be finished by the single DOF FTS. Theoretically, the multi-DOF FTS can fulfill machining more complex surfaces [17,18].

Therefore, developing multi-DOF FTS based on the single DOF FTS is the inevitable trend. [19,20] The flexible hinge has many advantages, such as no friction, no gap, no noise, high sensitivity and stable operation and it is widely used in FTS device [21,22]. However, most of the three DOF FTS devices have been developed are using serial mechanism with flexure hinge [17,23]. Although it met a part of the demand of the precision machining, there are some disadvantages such as complex institutions and low stiffness. Therefore, the FTS device designed in this paper will spurn the serial mechanism with fixed slide rail and put forward to use a 3-PUU (3 represents three branched chains, P represents prismatic pair, U represents hook hinge) parallel mechanism has more simple structure, more large stiffness, stronger carrying capacity and higher accuracy.

In this paper, the main contribution is the development

and control of a novel 3-DOF FTS device based on the 3-PUU parallel mechanism. The main content is: 1) FTS device's overall layout and structure design and modeling; 2) FTS device characterization of statics analysis and modal analysis; 3) experimental system open-loop and closed-loop controlling tests; 4) achievements are concluded with further work indicated.

2 Mechanism design and modeling

To cater for the requirements, a FTS system with 3-DOF has been designed in this paper, and it make the tool move freely on the three directions, so as to realize active control and error compensation in three directions (see Fig. 1).

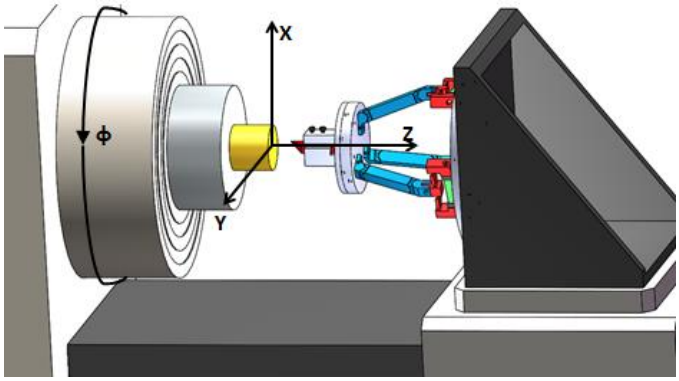

Fig. 1 Fast tool servo machining.

2.1 Design of 3-PUU parallel mechanism

In order to achieve the translational motion of tool in three directions, the FTS device designed in this paper use a 3-PUU 3-DOF translational parallel mechanism.

As shown in Fig. 2(a), the FTS device is made up of a tool, an upper platform, a lower platform, three branched chains and three piezoelectric actuators. Three branched chains with same structure connect the upper platform to the lower platform. All branched chains are related to P, U, U and connecting rod, as shown in Fig.3. Based on screw theory [24], it can be demonstrated that the novel FTS device can be arranged to achieve 3-DOF translational motion with certain geometric conditions.

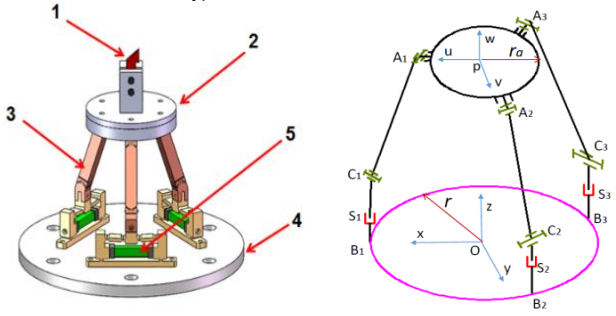

(a) (b)

Fig. 2 a) 3-PUU FTS mechanism. 1) Cutting tool; 2) The upper platform; 3) The branched chains; 4) The lower platform; 5) The piezoelectric actuator; b) Kinematics mathematical modeling of the 3-PUU FTS.

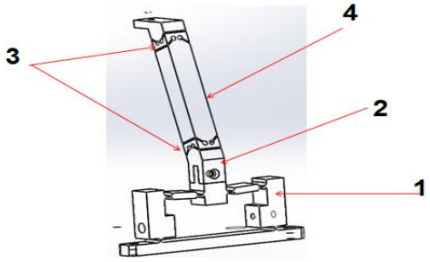

Fig. 3 The branched chain of the 3-PUU FTS mechanism. 1) Flexible displacement amplifier; 2) Prismatic pair; 3) Hook hinge; 4) Connecting rod.

Its kinematics mathematical modeling is show in Fig. 2(b). A coordinate system P (u, v, and w) is established on the movable platform, and a coordinate system O (x, y, and z) is established on the static plane. On the static plane, an equilateral triangle inscribed circle radius named *r,* and the circular radius on the movable plane named r_a.

In the P system, the position of each point is as follows:

$$A_1 = (r_a\,, 0\,, 0)$$

$$A_2 = (-\frac{r_a}{2}\,, \frac{\sqrt{3}r_a}{2}\,, 0)$$

$$A_3 = (-\frac{r_a}{2}\,, -\frac{\sqrt{3}r_a}{2}\,, 0)$$

In the O system, the position of each point is as follows:

$$C_1 = (r\,, 0\,, S_1\,)$$

$$C_2 = (\,-\frac{r}{2}, -\frac{\sqrt{3}r}{2}\,, S_2\,)$$

$$C_3 = (\,-\frac{r}{2}, -\frac{\sqrt{3}r}{2}\,, S_3\,)$$

Because the structure has translational motion in three directions and there is no relative rotation between moving coordinate system and foundational coordinate system, the displacement vector of the moving coordinate system can be expressed in the foundation as follows:

$$^{o}_{i}A = {}^{P}_{i}A + P\ (i = 1,2,3) \quad (1)$$

The length of the connecting rod *s* fixed length *L*. We can get three equations:

$$(x + r_a - r)^2 + y^2 + (Z - S_1)^2 = L^2 \quad (2)$$

$$(x - \frac{r_a}{2} + \frac{r}{2})^2 + (y + \frac{\sqrt{3}}{2}r_a - \frac{\sqrt{3}}{2}r)^2 + (Z - S_2)^2 = L^2 \quad (3)$$

$$(x - \frac{r_a}{2} + \frac{r}{2})^2 + (y - \frac{\sqrt{3}}{2}ra + \frac{\sqrt{3}}{2}r)^2 + (Z - S_3)^2 = L^2 \quad (4)$$

The S_1, S_2, S_3 is the distance between hook hinge and the static plane. Because $0 < S_i (i = 1,2,3) < z$, we can find out the solution of the formula (1) (2) (3):

$$\begin{cases} S_1 = -\sqrt{L^2 - r^2 + 2rr_a - r_a^2 + 2rx - 2r_ax - x^2 - y^2} + z \\ S_2 = -\sqrt{L^2 - r^2 + 2rr_a - r_a^2 - rx + r_ax - x^2 + \sqrt{3}ry - \sqrt{3}r_ay - y^2} + z \\ S_3 = -\sqrt{L^2 - r^2 + 2rr_a - r_a^2 - rx + r_ax - x^2 - \sqrt{3}ry + \sqrt{3}r_ay - y^2} + z \end{cases} \quad (5)$$

Taking the derivatives for (5), then,

$$\frac{\partial S_1}{\partial x} = -\frac{2r - 2r_a - 2x}{2\sqrt{L^2 - r^2 + 2rr_a - r_a^2 + 2rx - 2r_ax - x^2 - y^2}}$$

$$\frac{\partial S_1}{\partial y}=\frac{y}{\sqrt{L^2-r^2+2rr_a-r_a{}^2+2rx-2r_ax-x^2-y^2}}$$

$$\frac{\partial S_1}{\partial z}=1$$

$$\frac{\partial S_2}{\partial x}=-\frac{-r+r_a-2x}{2\sqrt{L^2-r^2+2rr_a-r_a{}^2-rx+r_ax-x^2+\sqrt{3}ry-\sqrt{3}r_ay-y^2}}$$

$$\frac{\partial S_2}{\partial y}=-\frac{\sqrt{3}r-\sqrt{3}\mathrm{ra}-2y}{2\sqrt{L^2-r^2+2rr_a-r_a{}^2-rx+r_ax-x^2+\sqrt{3}ry-\sqrt{3}r_ay-y^2}}$$

$$\frac{\partial S_2}{\partial z}=1$$

$$\frac{\partial S_3}{\partial x}=-\frac{-r+r_a-2x}{2\sqrt{L^2-r^2+2rr_a-r_a{}^2-rx+r_ax-x^2-\sqrt{3}ry+\sqrt{3}r_ay-y^2}}$$

$$\frac{\partial S_3}{\partial y}=-\frac{-\sqrt{3}r+\sqrt{3}r_a-2y}{2\sqrt{L^2-r^2+2rr_a-r_a{}^2-rx+r_ax-x^2-\sqrt{3}ry+\sqrt{3}r_ay-y^2}}$$

$$\frac{\partial S_3}{\partial z}=1$$

In the above formula, let's define

$$\mathrm{m}=\sqrt{\mathrm{L}^2-\mathrm{r}^2+2\mathrm{r}r_a-r_a{}^2+2\mathrm{rx}-2r_a\mathrm{x}-\mathrm{x}^2-\mathrm{y}^2}$$

$$\mathrm{n}=\sqrt{\mathrm{L}^2-\mathrm{r}^2+2\mathrm{r}r_a-r_a{}^2-\mathrm{rx}+r_a\mathrm{x}-\mathrm{x}^2+\sqrt{3}\mathrm{ry}-\sqrt{3}r_a\mathrm{y}-\mathrm{y}^2}$$

$$\mathrm{t}=\sqrt{\mathrm{L}^2-\mathrm{r}^2+2\mathrm{r}r_a-r_a{}^2-\mathrm{rx}+r_a\mathrm{x}-\mathrm{x}^2-\sqrt{3}\mathrm{ry}+\sqrt{3}r_a\mathrm{y}-\mathrm{y}^2}$$

Therefore, we obtain

$$\begin{bmatrix}\Delta S1\\ \Delta S2\\ \Delta S3\end{bmatrix}=\begin{bmatrix}-\frac{2\mathrm{r}-2r_a-2\mathrm{x}}{2\mathrm{m}} & \frac{\mathrm{y}}{\mathrm{m}} & 1\\ -\frac{-\mathrm{r}+r_a-2\mathrm{x}}{2\mathrm{n}} & -\frac{\sqrt{3}\mathrm{r}-\sqrt{3}r_a-2\mathrm{y}}{2\mathrm{n}} & 1\\ -\frac{-\mathrm{r}+r_a-2\mathrm{x}}{2\mathrm{t}} & -\frac{-\sqrt{3}\mathrm{r}+\sqrt{3}r_a-2\mathrm{y}}{2\mathrm{t}} & 1\end{bmatrix}\begin{bmatrix}\Delta\mathrm{x}\\ \Delta\mathrm{y}\\ \Delta\mathrm{z}\end{bmatrix} \quad (6)$$

We can know

$$\mathbf{J}=\begin{bmatrix}-\frac{2\mathrm{r}-2r_a-2\mathrm{x}}{2\mathrm{m}} & \frac{\mathrm{y}}{\mathrm{m}} & 1\\ -\frac{-\mathrm{r}+r_a-2\mathrm{x}}{2\mathrm{n}} & -\frac{\sqrt{3}\mathrm{r}-\sqrt{3}r_a-2\mathrm{y}}{2\mathrm{n}} & 1\\ -\frac{-\mathrm{r}+r_a-2\mathrm{x}}{2\mathrm{t}} & -\frac{-\sqrt{3}\mathrm{r}+\sqrt{3}r_a-2\mathrm{y}}{2\mathrm{t}} & 1\end{bmatrix} \quad (7)$$

Among them, **J** is the Jacobi matrix of the 3-PUU FTS mechanism.

2.2 The design of flexible displacement amplifier

High precision piezoelectric ceramic actuators are used as a driving element in the FTS device designed in this paper. However, the stroke of piezoelectric ceramic is small. In order to enlarge the stroke of device, flexible displacement amplifier is used to magnify the output displacement of the PZT, as shown in Fig. 4.

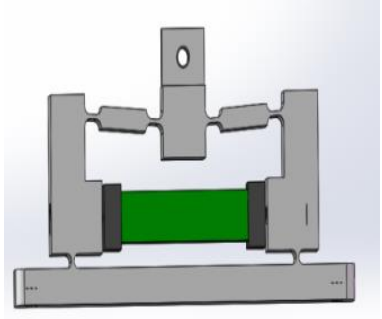

Fig. 4 Flexible displacement amplifier.

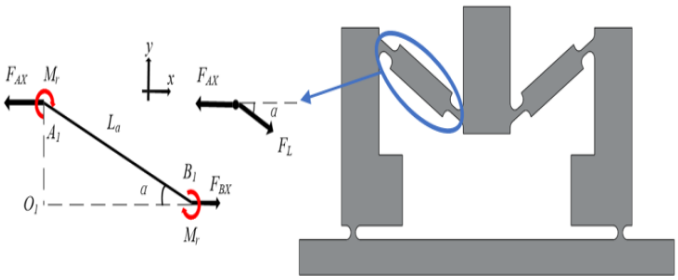

Fig. 5 Half of the compound bridge-type amplifier.

By the force equilibrium along the x-axis in Fig.5, we can get that $F_{AX}=F_{BX}=F_X$, to calculate the moment equilibrium at point A_1, the following relation can be obtained:

$$F_X L_a \sin\alpha = 2M_r = 2K_r\Delta\alpha \quad (8)$$

where M_r is the moment arising from the rotational stiffness K_r of the flexure hinge and the induced rotational deformation $\Delta\alpha$. K_r is the translational stiffness of one flexure hinge.

The internal force in the leg $\mathrm{A}_1\mathrm{B}_1$ is:

$$F_L=\frac{F_X}{cos}\alpha=K_t\Delta L \quad (9)$$

where ΔL is the linear deformation caused by the translational stiffness K_t of the flexure hinge.

Based on the virtual work principle, we can get the following relationship:

$$F_X\Delta x=F_L\Delta L+2M_r\Delta\alpha \quad (10)$$

By Eps. (8) and (9), the relationship Ep.(10) can be expressed as:

$$\Delta x=K_t\Delta L^2+2K_r\Delta\alpha^2 \quad (11)$$

Solving $\Delta\alpha$ and ΔL and then inserting them into (11):

$$\Delta x=\frac{2K_r+K_tL_a^2cos^2\alpha sin^2\alpha}{2K_rK_tcos^2\alpha} \quad (12)$$

$$y=\int L_a\sin\alpha\,dt \quad (13)$$

$$\Delta y=L_a\cos\alpha\,\Delta\alpha \quad (14)$$

Substituting $\Delta\alpha$ into Ep. (14):

$$\Delta y=\frac{L_a^2\cos\alpha\sin\alpha}{2K_r}F_X \quad (15)$$

$$A_2=\frac{\Delta y}{\Delta x}=\frac{K_tL_\alpha^2cos\alpha^3\sin\alpha}{2K_r+K_tL_\alpha^2\cos\alpha^2\sin\alpha^2} \quad (16)$$

$$K_{in}=\frac{2F_x}{\Delta x}=\frac{4K_tK_r(\cos\alpha)^2}{2K_r+K_tL_a^2cos^2\alpha sin^2\alpha} \quad (17)$$

$A_2$is the amplification ratio of bridge-type amplifier. K_{in} is the input stiffness of the bridge-type, and it is equal to the output stiffness of the lever.

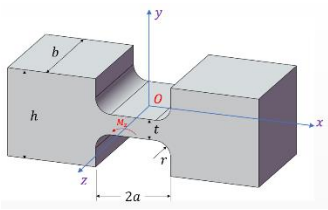

Fig. 6 Corner-filleted hinge

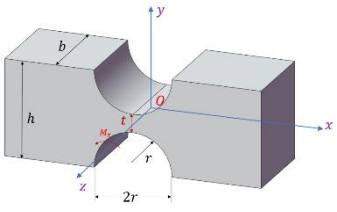

Fig. 7 Right circular hinge

For corner-filleted flexible hinge, $\beta = \frac{t}{2r}$, $\gamma = \frac{t}{2a}$

For right circular flexible hinge, $\alpha = \frac{t}{2r}$, $\psi = \frac{h}{2r}$

Also, the rotational stiffness of the corner-filleted flexible hinge can be derived as follows,

$$K = \frac{Ebt^3r^2}{12lr^2+12ft^3} \tag{18}$$

where r is the fillet radius, E is the elastic modulus of the material,

$$f = \int_{-\frac{\pi}{2}}^{\frac{\pi}{2}} \frac{\cos\theta}{\left(\frac{t}{r}+2-2\cos\theta\right)^3} d\theta \tag{19}$$

Afterwards, the displacement relationship of flexure hinge can be expressed as follows,

$$\begin{bmatrix} \theta \\ \Delta y \\ \Delta x \end{bmatrix} = \begin{bmatrix} C_{\theta,M_z} & C_{\theta,F_y} & 0 \\ C_{y,M_z} & C_{y,F_y} & 0 \\ 0 & 0 & C_{x,F_x} \end{bmatrix} \begin{bmatrix} M_z \\ F_y \\ F_x \end{bmatrix} \tag{20}$$

where $C_{\theta,M_z} = \frac{12}{Eb}(f_1' + f_1'')$

$C_{\theta,F_y} = C_{y,M_z} = \frac{12}{Eb}(af_1' + af_1'' - f_2' - f_2'')$

$C_{y,F_y} = \frac{12}{Eb}(a^2f_1' + a^2f_1'' - 2af_2' - 2af_2'' + f_3' + f_3'')$

$C_{x,F_x} = \frac{1}{Eb}(f_4' + f_4'')$

For corner-filleted flexible hinge,

$$f_1' = f_1'' = \frac{1}{4t^2}\left[\frac{2}{\gamma} - \frac{2}{\beta} + \frac{2\beta^2+4\beta+3}{(\beta+1)(\beta+2)^2} + \frac{6(\beta+1)}{\sqrt{\beta}(\beta+2)^{2.5}} tan^{-1}\sqrt{\frac{2}{\beta}+1}\right] \tag{21}$$

$$f_2' = f_2'' = -\frac{1}{8t\beta}\left\{\frac{\beta-\gamma}{(\beta+2)^2\gamma}\left[\frac{2\beta^2+4\beta+3}{(\beta+1)(\beta+2)^2} + \frac{6(\beta+1)}{\sqrt{\beta}(\beta+2)}\tan^{-1}\sqrt{\frac{2}{\beta}+1}\right] + \frac{1}{\beta+1}\right\} - \tag{22}$$

$$f_3' = f_3'' = -\frac{1}{16\gamma^2}\left[\frac{2}{\gamma} - \frac{2}{\beta} + \frac{2\beta^2+4\beta+3}{(\beta+1)(\beta+2)^2} + \frac{6(\beta+1)}{\sqrt{\beta}(\beta+2)^{2.5}} tan^{-1}\sqrt{\frac{2}{\beta}+1}\right] + \frac{1}{8}\left\{\frac{(\beta-\gamma)(4\beta^2-2\beta\gamma+\gamma^2)}{3\beta^3\gamma^3} + \frac{2\beta^2+4\beta+3}{(\beta+1)(\beta+2)^2\gamma^2} + \frac{2\beta^3+6\beta^2+3\beta-5+2\beta(1-\beta)/\gamma}{2[\beta(\beta+2)]^2} + \frac{(\beta+1)(3+2\beta-7\beta^2-8\beta^3-2\beta^4+6\beta^2/\gamma^2-6\beta/\gamma)}{[\beta(\beta+2)]^{2.5}} tan^{-1}\sqrt{\frac{2}{\beta}+1} + \frac{\pi}{2}\right\} \tag{23}$$

$$f_4' = f_4'' = \frac{\beta-\gamma}{2\beta\gamma} + \frac{\beta+1}{\sqrt{\beta}(\beta+2)}\tan^{-1}\sqrt{\frac{2}{\beta}+1} - \frac{\pi}{4} \tag{24}$$

The parameters without superscript denotes the analyzed lever, while the parameters with superscript " ' " denotes the first lever, the parameters with superscript " " " denotes the second one.

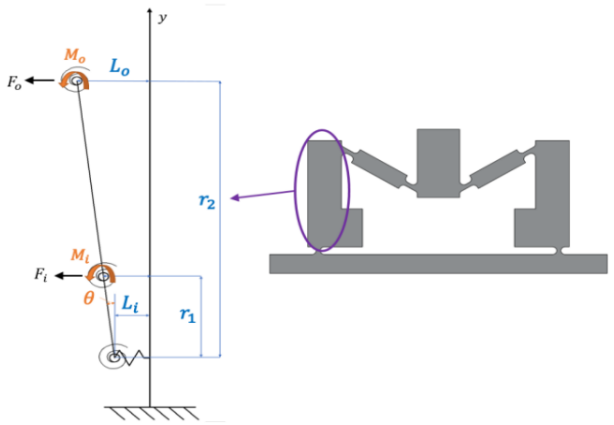

Fig. 8 The output lever model of flexible displacement amplifier.

From (18), we gain

$$\Delta y = F_iY_1 + F_oY_2 + M_zC_{y,M_z} \tag{25}$$

$$\theta = F_iY_3 + F_oY_4 + M_zC_{\theta,M_z} \tag{26}$$

where $M_z = M_i + M_o, Y_1 = C_{y,F_y} + r_1C_{y,M_z}$, $Y_2 = C_{y,F_y} + r_2C_{y,M_z}$ $Y_3 = C_{\theta,F_y} + r_1C_{\theta,M_z}, Y_4 = C_{\theta,F_y} + r_2C_{\theta,M_z}, r_1 = R_1 - a, r_2 = R_2 - a$

From geometrical relationship (see Fig.8), we get

$$\theta = \frac{L_i - \Delta y}{r_1} \tag{27}$$

$$L_o = \Delta y + r_2\theta \tag{28}$$

$$M_i = -K(\theta + \frac{L_i}{r_2'}) \tag{29}$$

$$M_o = -K(\theta + \frac{L_o}{r_1''}) \tag{30}$$

From (25) to (30), we get

$$\Delta y = \frac{Y_5+Y_6}{Y_5+Y_7}L_i + \frac{Y_2Y_3-Y_1Y_4}{Y_3(Y_5+Y_7)}F_o \tag{31}$$

$$\theta = \frac{Y_7-Y_6}{r_1(Y_7+Y_5)}L_i - \frac{Y_2Y_3-Y_1Y_4}{r_1Y_3(Y_5+Y_7)}F_o \tag{32}$$

$$L_o = Y_8L_i + Y_9F_o \tag{33}$$

$$F_i = Y_{10}L_i - Y_{11}F_o \tag{34}$$

where $Y_5 = \frac{Y_1+(p_i+p_o)(Y_1-C_{y,M_z}KY_3)}{r_1Y_3}$ (35)

$$Y_6 = -\frac{C_{y,M_z}KY_3-Y_1}{Y_3}\left(\frac{1}{q_ir_2'} + \frac{m}{q_or_1''}\right) \tag{36}$$

$$Y_7 = 1 + \frac{C_{y,M_z}KY_3-Y_1}{q_or_1''Y_3}(1-m) \tag{37}$$

$$Y_8 = \frac{Y_5+Y_6+m(Y_7-Y_6)}{Y_5+Y_7} \tag{38}$$

$$Y_9 = \frac{(1-m)(Y_2Y_3-Y_1Y_4)}{Y_3(Y_5+Y_7)} \tag{39}$$

$$Y_{10} = \frac{(1+p_i+p_o)(Y_7-Y_6)}{r_1Y_3(Y_5+Y_7)} + \frac{1}{Y_3}\left(\frac{1}{q_ir_2'} + \frac{Y_8}{q_or_1''}\right) \tag{40}$$

$$Y_{11} = \frac{(1+p_i+p_o)(Y_2Y_3-Y_1Y_4)}{r_1Y_3^2(Y_5+Y_7)} + \frac{Y_4}{Y_3} - \frac{Y_9}{q_or_1''Y_3} \tag{41}$$

$$m = \frac{r_2}{r_1} \tag{42}$$

When the lever relative to the flexure hinge rotating, p_i and p_o are equal to 1. When the lever relative to the flexure hinge rotating in the opposite direction, q_i and q_o are equal to 1.

Finally, the displacement amplification ratio of the output lever A_2 is derived as follows,

$$A_1 = \frac{L_o}{L_i} = \frac{(K_{in}-Y_9)Y_8}{K_{in}} \quad (43)$$

$$A = A_1 A_2 == \frac{(K_{in}-Y_9)Y_8}{K_{in}} \frac{K_t L_\alpha^2 cos\alpha^3 \sin\alpha}{2K_r+K_t L_\alpha^2 \cos\alpha^2 \sin\alpha^2} \quad (44)$$

2.3 The workspace calculation

Workspace is the motion range of the tool which can be achieved, and workspace is one of the important index of FTS device. Using Monte Carlo method (also called boundary search method), we can find out the working space. Its principle is as follows: a scope contains all possible workspace, then millions of points is generated in this scope. Each point would be tested whether the point is within the workspace. After searching all eligible points out, these points make up the workspace of the FTS device. L=60mm, r =70.00mm, r_a=27mm, and $0<S_i<$ 0.25mm, MATLAB is used to search for workspace, the workspace can be obtained as follows,

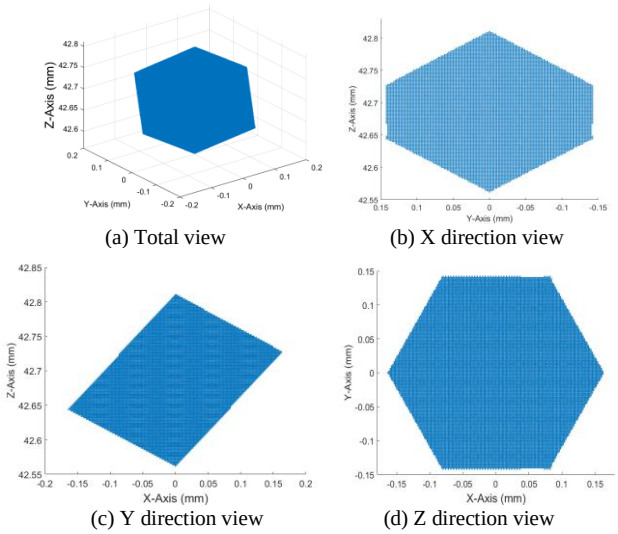

(a) Total view (b) X direction view

(c) Y direction view (d) Z direction view

Fig. 9 The workspace of the FTS.

3 Fea analysis

In this section, the optimized mechanism performance is validated by the ANSYS Workbench. A new project is created with the new material parameters of (Young's modulus) =71.7GPa, (yield strength) = 503MPa, (Poisson's ratio)=0.33, (density)=2810Kg/m3. Then a 3D finite element model is established with the 3D software Solidworks. A fixed support is exerted onto the established model to immobilize the 3D mechanism model. Then, the FEA tests in terms of prismatic motion analysis, stress analysis, the displacement magnification analysis, rotation angle analysis, and modal analysis are conducted in detail.

3.1 Static structural analysis

Firstly, to test the strain response performance of this mechanism, a set of forces 0~1600N are exerted at the three driving points synchronously. As shown in Table 1, it is observed that the relationship between the output displacement and the input force is linear. Besides, to test the displacement magnification performance of this mechanism, a set of input displacements 5μm, 10μm, 15μm, 20μm, 25μm, 30μm, and 35μm are exerted at the three driving points synchronously. As shown in Table 2, it can be observed that the value of the displacement magnification is not influenced by the input displacement; also, the displacement amplification ratio can be calculated as around 4.1.

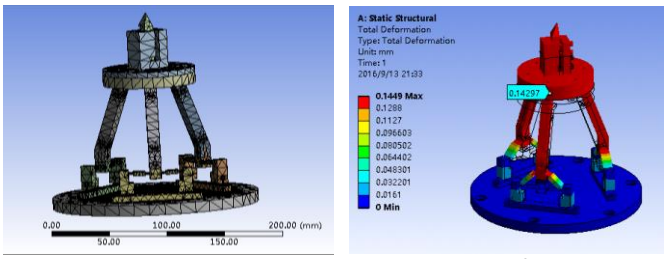

(a) 3D FEA model (b) The total deformation

Fig. 10 The static structural analysis results.

Table 1 The output displacement in terms of the variation of the input force

F/N	δ_{out}/mm	σ_{max} /MPa	A
100	0.018	23.8	4.7
200	0.035	47.5	4.7
400	0.071	95.0	4.7
800	0.143	190.2	4.8
1600	0.282	380.3	4.8

Table 2 The output displacement in terms of the variation of the input displacement

δ_{in}/mm	δ_{out}/mm	σ_{max} /MPa	A
0.005	0.0201	34.876	4.0
0.010	0.0412	69.751	4.1
0.015	0.0610	104.63	4.1
0.020	0.0824	139.52	4.1
0.025	0.1022	174.38	4.1
0.030	0.1231	209.25	4.1
0.035	0.1434	244.13	4.1

3.2 Modal analysis

Furthermore, its dynamic performance is verified through the modal analysis. As shown in Fig. 11 (a-f), the first mode shape is displayed with its resonance frequency, where the red and the blue color represent the maximum and the minimum output displacement, respectively. It indicates that the presented FTS possesses a high working frequency (66Hz). In addition, the other motion mode resonance occurs at the mode 2~6, the resonance frequencies are much higher than 66Hz. All the FEA results further confirmed that the proposed FTS device has an excellent performance for fulfilling precision positioning task.

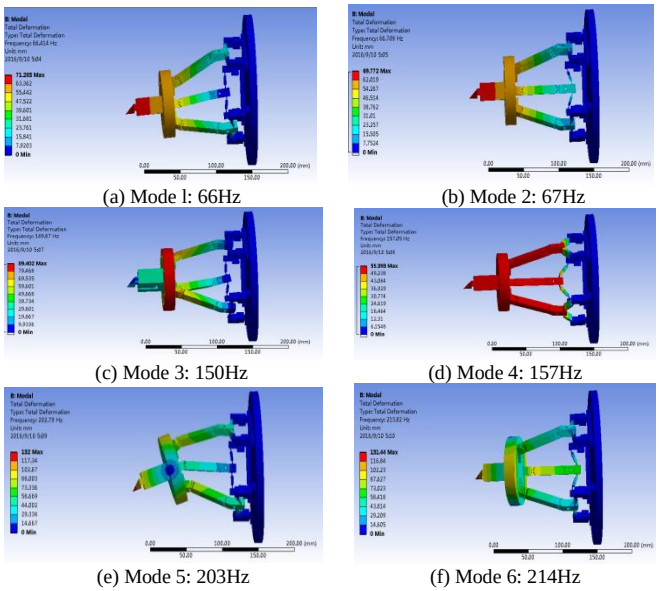

(a) Mode l: 66Hz (b) Mode 2: 67Hz

(c) Mode 3: 150Hz (d) Mode 4: 157Hz

(e) Mode 5: 203Hz (f) Mode 6: 214Hz

Fig. 11 The first six mode shapes of the FTS device FEA model

4 Hysteresis modeling with Modified Prandtl-Ishlinskii Model

Piezoelectric actuator has inherent hysteresis nonlinearity. It is necessary to model and compensate for the adverse effects of micro/nano control. In view of the hysteresis phenomenon, many domestic and foreign scholars have proposed a number of hysteresis modeling methods, in which the most popular model is Prandtl-Ishlinskii(PI) model [24]. The linear superposition of the play operator similar to the hysteresis loop is used to describe the hysteresis. In various hysteresis models, PI model has been widely adopted due to its easy to analyze and obtain the inverse solution. In practice, it is too ideal since the symmetry operators are hard to describe the complex hysteresis behavior. In this work, a modified PI model with non-symmetry operator is proposed to enhance the positioning performance.

4.1 Construction of PI operator

As a classical mathematical model, it is widely used in the field of hysteretic nonlinear research. It is formed by linear weighting of play operators with different thresholds. Play operator is the basic element of hysteresis model. The mathematical expressions are expressed as follows:

$$\varphi[k]=\max\{u[k]-r,\min\{u[k]+r,v[k-1]\}\}(k=1,\ldots,N) \quad (37)$$

$$\varphi[0]=\max\{v[k]-r,\min\{v[k]+r,0\}\} \quad (38)$$

where $r^T=(r_1,\ldots,r_n)$ is the threshold, and the value $r=(\mathrm{i}-1)/n*\max|\mathrm{u}[k]|$, n is the number of operators. The schematic diagram of PI operator is displayed as follows,

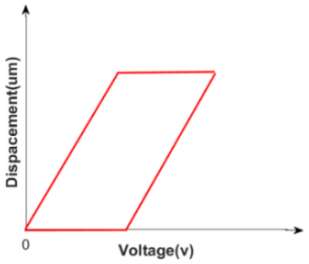

Fig. 12 The schematic of PI operator

4.2 Construction of PI model

Firstly, the input voltage range of the piezoelectric actuator is [$u_{\min}$, $u_{\max}$]. The output voltage range of the piezoelectric actuator is the schematic of PI operator. Because the actual input voltage is controlled by digital control, it is considered that output voltage v[k-1] at the time of k-1 and the output voltage v[k] at the time of k are monotonic. Therefore, the output of PI model at k time can be expressed as a linear weighted superposition of several different PI operators, and the output formula of PI hysteresis model can be obtained:

$$v[k]=W\varphi=\sum_{i=1}^{n}w_i*\max\{u[k]-r_i,\min\{u[k]+r_i,v[k-1]\}\}(k=1,\ldots,N) \quad (39)$$

where $W^T=(w_1,\ldots,w_n)$ is the weight coefficient, $r^T=(r_1,\ldots,r_n)$ is the threshold, its selection is of in accordance with $r=(\mathrm{i}-1)/n*\max|\mathrm{u}[k]|$, where n is the number of operators.

4.3 Construction and Identification of Modified PI Model

The operator of the traditional PI model has strong odd symmetry, however, the hysteresis loops are often non symmetric, which lead to the fitting accuracy of the PI model is severely limited. In order to overcome this shortcoming, the traditional PI model should be improved. Here, a type of operator with the property of non-odd symmetry is proposed to build up a modified PI model(MPI). This saturation operator is a weighted linear superposition of linear-stop or one-sided dead-zone operators, that is,

$$\begin{aligned}S_d[v](k)&=\max\{v(k)-d,0\}(d>0)\\ S_d[v](k)&=v(k)(d=0)\end{aligned} \quad (40)$$

where $d^T=(d_1,\ldots,d_n)$ is threshold, and

$$d=(\mathrm{i}-1)/n*\max|v[k]| \quad (41)$$

n is the number of operators.

Therefore, the output of the MPI model at the time of k can be expressed as a linear weighted superposition of

several different PI improved operators. The output formula of modified PI(MPI) hysteresis model [26-27] can be described as follows,

$$y = WS_d[v](k) = WS_d[W\varphi](k) \tag{42}$$

The least squares method is used to identify the MPI weight coefficient, then, the weight coefficient of the MPI model can be derived as follows,

$$S_d W = y \rightarrow S_d{}^T S_d W = S_d{}^T y \rightarrow W = (S_d{}^T S_d)^{-1} S_d{}^T y \tag{43}$$

The modified model, that is, the MPI model, can effectively overcome the asymmetry of the hysteresis loop compared to the traditional PI model. For irregular hysteresis loops, the good tracking prediction accuracy can be obtained. Because it uses the least square method to identify, the weights can be solved step by step theoretically. The algorithm is relatively simple. And the response speed is relatively fast. It is easy to implement online real-time function.

5 Experimental system and test results

In this section, open loop testing is used to verify the performance of the FTS device such as the displacement amplification ratio and the hysteresis effect. And a new closed-loop controller composed of an inverted MPI model and a new repetitive-compensated PID controller is proposed to enhance the positioning performance of the FTS. The experimental system is established as shown in Fig.13.

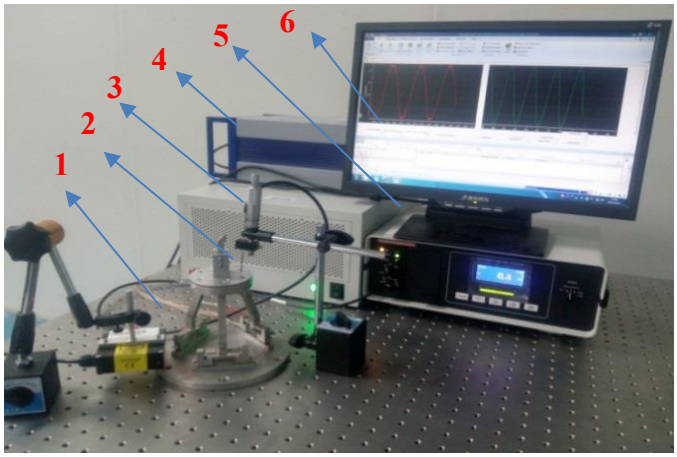

Fig.13 The experimental system. 1) Laser displacement sensor, 2) 3-PUU FTS device, 3) dSPACE control system, 4) The voltage amplifier, 5) MTI-2100, 6) Host computer.

5.1 Test of the displacement amplification ratio

A time-varying voltage is applied on the piezoelectric actuator installed in the flexible displacement amplifier. The input and output displacement are measured through the displacement sensor, respectively. As shown in Fig.14. the displacement amplification ratio(A=Output displacement/Input displacement) can be calculated as about 3.87.

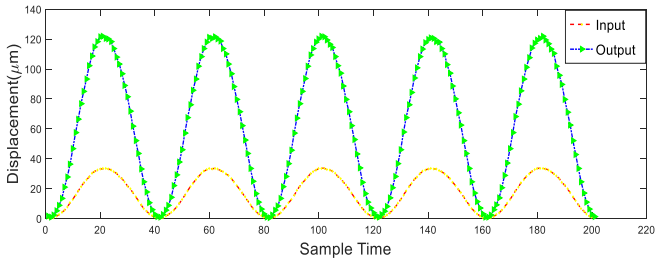

Fig.14 The measured input and output displacements.

5.2 Open-loop test of the FTS

A time-varying voltage is applied simultaneously on the three piezoelectric actuators. The driving voltage-time curve is shown in Fig.15(a). Accordingly, the displacement of the mobile platform will produce change over time in the Z direction. As shown in Fig.15(b), the displacement-time curve is measured and plotted with the displacement sensor.

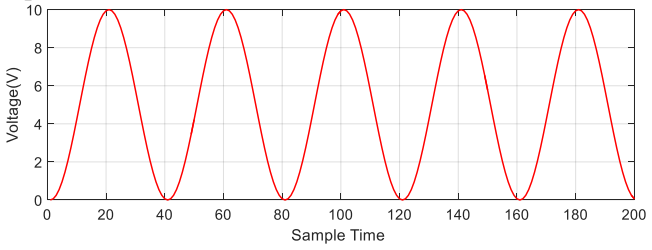

a)

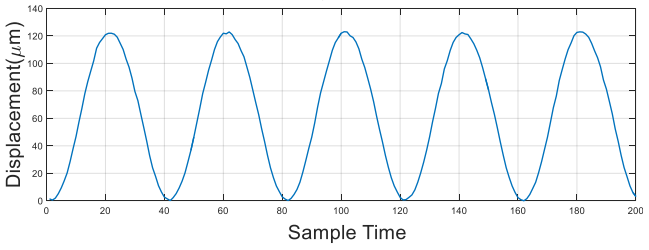

b)

Fig. 15 The open-loop testing results of the 3-PUU FTS mechanism in Z-axis. a) The driving voltage, b) The measured output displacement.

The experimental results indicate that the motion range of the FTS device in Z direction is around 0~120μm. Herewith, the motion ranges of the other two directions have been measured. The motion range in X direction is about -80μm to 80μm and in Y direction is about -85μm to 85μm. As shown in Fig.16, the hysteresis nonlinearity curve are plotted and displayed.

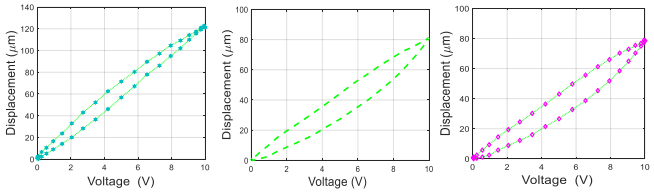

(a) (b) (c)

Fig. 16 a) Hysteresis effect in X-axis, b) Hysteresis effect in Y-axis. c) Hysteresis effect in Z-axis.

In this paper, a set of test data is used to verify the accuracy of the hysteresis model based on MPI model. Then, the identification results of the PI modes and MPI

model are shown in Fig.17. A variable frequency amplitude signal is applied to the PZT actuator. We can get the output displacement curve as shown in Fig17(a). Using the PI and MPI model to identify the displacement curve, we can obtain the fitting curves, as shown in Fig17(b) and Fig17(c). By calculating the difference between the two curves, the fitting errors diagram of the PI and MPI model can be obtained as shown in Fig17(d). According to the model identification results, it can be seen that the identification errors decrease with the decreasing of amplitude. The maximum identification error of the MPI model and the PI model is about 800nm and 3μm, respectively. Therefore, the performance of MPI model is obviously better than the PI model when the hysteresis loop is nonsymmetric. The MPI model has enough accuracy to be applied to the control system.

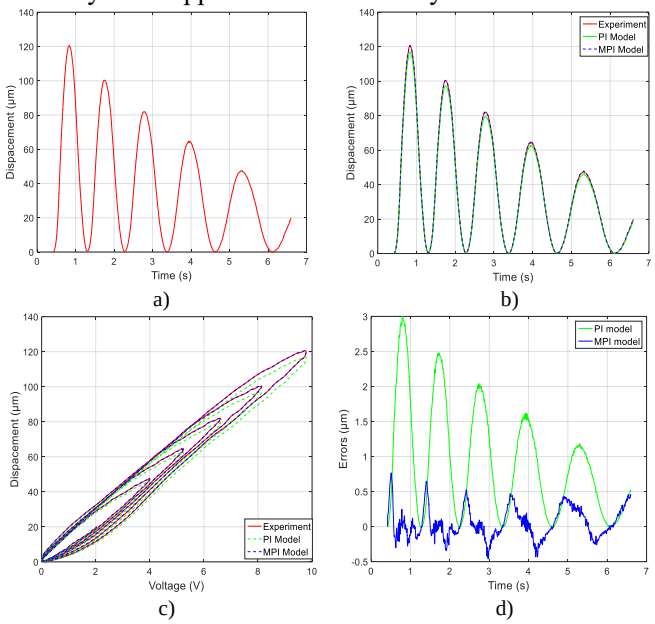

Fig. 17 The results of the identified PI and MPI hysteresis model. (a) The experimental displacement; (b) The experimental result and the two model output; (c) The displacement-voltage hysteresis loops; (d) The errors of PI model and MPI model output.

5.3 Closed-loop test of the FTS

As shown in Fig.11, The input voltage of the piezoelectric ceramics and the output displacement of each direction of the FTS mechanism exhibit an obvious hysteresis nonlinearity, which is greatly reduce the positioning accuracy of the FTS system. As shown in Fig.18, in order to reduce the error and improve the control precision, a new closed-loop controller composed of an inverted MPI model and a new repetitive-compensated PID controller is here proposed, which aims to enhance the positioning performance of the FTS mechanism.

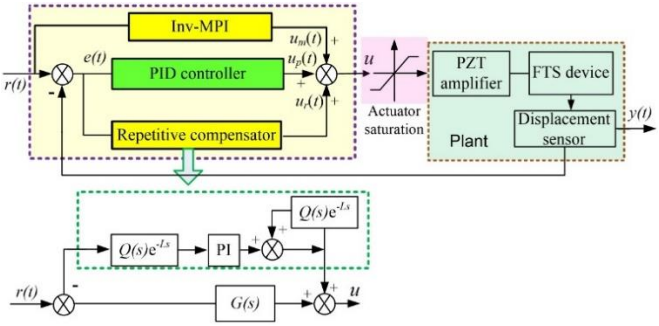

Fig. 18 The designed closed-loop controller.

As an example in Z axis, the fixed-step size (sample time) is set to 0.001s, and the controller parameters are assigned as follows: Kp=0.01, k_i=60, k_d =0.00001(PID controller); Kp=0.5, k_i=12 (repetitive-compensator), the reference signal and the output displacement of Z axis are shown in the Fig.19(a). It indicates that the maximum error is kept within 600nm, while the hysteresis nonlinearity is successfully e

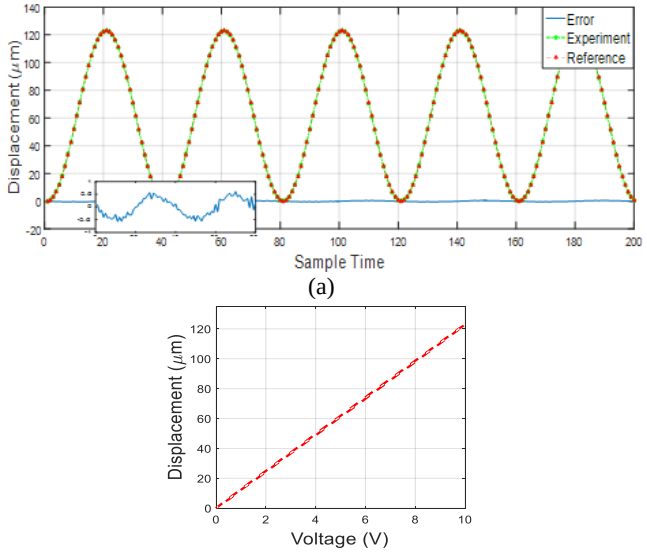

Fig.19 The closed-loop testing results of the 3-PUU FTS mechanism in Z-axis. a) The reference signal and the output displacement; b) The linearized hysteresis nonlinearity effect.

6 Conclusions

In this paper, a novel compliant fast tool servo device for ultra-precision machining has been proposed. Firstly, in view of the requirements of cutting error compensation in X, Y and Z axis in complex microstructural surface machining, a flexure-based and decoupled 3-PUU FTS device with precision motions is designed, and the kinematics modeling is carried out. Besides, finite element analysis is carried out to validate the static and dynamic performance of the FTS device. In the case of the reciprocation movement of FTS, a new repetitive-compensated PID controller combined with an

inverted modified Prandtl-Ishlinskii model is designed to improve the repetitive positioning performance. A series of cutting trajectory tracking experiments are carried out via dSPACE rapid prototype controlling system.

In conclusion, a workspace of [-85, 85]∪[-80,80]∪[0,120]μm^3 has been achieved. Also, its closed-loop positioning precision can reach up to 600nm. It indicates that the proposed FTS device has a large working stroke and a high enough accuracy. Besides, this device adopts a parallel mechanism to make it simpler in structure than the existing devices. Thus, it has a better application prospect. Its satisfactory performance make it will be considered to be employed in the practical microstructural cutting tasks in out near further work.

Acknowledgments This work was supported in part by Natural Science Foundation of China (5160051494, U1601202), Science and Technology Program of Guangzhou (201510010058), Natural Science Foundation of Guangdong (2014A030310204), Guangdong General Programs for Science and Technology (2015A010104009, 2015B010104008, 2015B010133005).

References

1. Brecher C, Lange S, Merz M, Niehaus F, Wenzel C, Winterschladen M, Wech M (2006) NURBS based ultra-precision free-form machining. CIRP Ann: Manuf Technol 55: 547–550.
2. Fang FZ, Zhang XD, Weckenmann A, Zhang GX, Evans C (2013)Manufacturing and measurement of freeform optics. CIRP Annals-Manufacturing Technology 62:823–846.
3. Tao F, Cheng JF, Qi QL, Zhang M, Zhang H, Sui FY (2017) Digital twin driven product design, manufacturing and service with big data. International Journal of Advanced Manufacturing Technology DOI: 10.1007/s00170-017-0233-1.
4. Oliveira OG, Lima Monteiro DW, Costa RFO (2014) Optimized microlens-array geometry for Hartmann-Shack wavefront sensor. Opt. Laser Eng 55:155–161.
5. Ow YS, Breese MBH, Azimi S (2010) Fabrication of concave silicon micro-mirrors. Opt. Express 18 (14): 14511-14518.
6. Wong S, GS Hong (2011) Optimal selection of machining parameters for fast tool servo diamond turning. The International Journal of Advanced Manufacturing Technology 57(1-4):85~99.
7. Tao F, Bi L, Zuo Y, Nee A (2017) A cooperative co-evolutionary algorithm for large-scale process planning with energy consideration, Journal of Manufacturing Science and Engineering-Transaction of the ASME, Vol.139(6):061016-1---061016-11.
8. Tao F, Cheng Y, Zhang L, Nee A (2017) Advanced manufacturing systems: socialization characteristics and trends. Journal of Intelligent Manufacturing 28(5):1079-1094.
9. Tao F, Qi QL (2017) New IT Driven Service-Oriented Smart Manufacturing: Framework and characteristics. IEEE Transactions on Systems, Man and Cybernetics: Systems, DOI: 10.1109/TSMC.2723764.
10. Oliveira OG, Lima Monteiro DW, Costa RFO (2014) Optimized microlens-array geometry for Hartmann-Shack wavefront sensor, Opt. Laser Eng 55:155–161.
11. Pan A, Gao B, Chen T, Si J, Li C, Chen F, Hou X (2014) Fabrication of concave spherical microlenses on silicon by femtosecond laser irradiation and mixed acid etching, Opt. Express 22 (12):15245–15250.
12. Lu X, Trumper DL (2005) Ultrafast tool servos for diamond turning. CIRP Ann: Manuf Technol 54: 383–8.
13. Sang HS， Lee KL, Lee KM, Bang YB (2009) Fabrication of free-form surfaces using a long-stroke fast tool servo and corrective figuring with on-machine measurement. International Journal of Machine Tools and Manufacture 49(12): 991–997.
14. Yu DP, Hong GS, Yoke San Wong (2011) Profile error compensation in fast tool servo diamond turning of micro-structured surfaces. International Journal of Machine Tools and Manufacture 52(1):13–23.
15. Scheiding S, Yi AY, Gebhardt A, Li L, Risse S, Eberhardt R, Tunnermann A(2011) Freeform manufacturing of a microoptical lens array on a steep curved substrate by use of a voice coil fast tool servo. Opt Express 19(24): 23938–51.
16. Zou Q, Yao JN, Wang T (2013) Analysis and Design of a 2-DOF Linear FTS Device. The International Conference on Advance in Construction Machinery and Vehicle Engineering ICACMVE'13.
17. Zhu ZW, Zhou XQ, Liu ZW, Wang RQ, Zhu L (2014) Development of a piezoelectrically actuated two-degree-of-freedom fast tool servo with decoupled motions for micro-/nanomachining. Precision Engineering 38(4):809-820.
18. Zhu ZW, To S, Kornel F, Ehmann, and Zhou XQ (2017) Design, analysis, and realization of a novel piezoelectrically actuated rotary spatial vibration system for micro-/nano-machining. IEEE/ASME Transactions on Mechatronics 22(3): 1227 –1237.
19. Tang H and Li Y (2015) Feedforward nonlinear PID control of a novel nanomanipulator using Preisach hysteresis compensator.Robotics and Computer-Integrated Manufacturing, 34: 124-132.
20. Tao F, Qi QL (2017) New IT Driven Service-Oriented Smart Manufacturing: Framework and characteristics. IEEE Transactions on Systems, Man and Cybernetics: Systems, DOI: 10.1109/TSMC.2017.2723764.
21. Tao F, Cheng J, Cheng Y, Gu S, Zheng TY, H Yang, SDM Sim (2017) A manufacturing service supply–demand matching simulator under cloud environment. Robotics and Computer Integrated Manufacturing, 45(6):34–46.
22. Tang H, Li Y (2015) A New Flexure-based Yθ Nanomanipulator with Nanometer Scale Positioning Resolution and Millimeter Range Workspace. IEEE-ASME Transactions on Mechatronics 20(3):1320–1330.
23. Wada T, Takahashi M, Moriwaki T, Nakamoto K (2007) Development of a three axis controlled fast tool servo for ultra precision machining (1st report). J Jpn Soc Precis Eng 73: 1345–9.
24. Wang H, and Zhang X (2008) Input coupling analysis and optimal design of a 3-DOF compliant micro-positioning stage. Mech. Mach. Theory 43 (4) 400-410.
25. Huang Z, Zhao YS, Zhao TS (2014) Advanced Spatial Mechanism. Beijing: Higher Education Press.
26. Eral HB, Mannetje DJCM', Oh J M (2013) Contact angle hysteresis: a review of fundamentals and applications[J]. Colloid and Polymer Science, 291(2): 247–260.
27. Chaipanich A, Jiatanong N, Yimnirun R (2009) Ferroelectric Hysteresis Behavior in 0-3 PZT-Cement Composites: Effects of Frequency and Electric Field. Ferroelectrics Letters Section 36(3-4): 59-66.